A Surface Mooring for Air–Sea Interaction Research in the Gulf Stream. Part II: Analysis of the Observations and Their Accuracies

SÉBASTIEN P. BIGORRE AND ROBERT A. WELLER

Woods Hole Oceanographic Institution, Woods Hole, Massachusetts

JAMES B. EDSON

Department of Marine Sciences, University of Connecticut, Storrs, Connecticut

JONATHAN D. WARE

Woods Hole Oceanographic Institution, Woods Hole, Massachusetts

(Manuscript received 21 April 2012, in final form 17 September 2012)

ABSTRACT

A surface mooring was deployed in the Gulf Stream for 15 months to investigate the role of air–sea interaction in mode water formation and other processes. The accuracies of the near-surface meteorological and oceanographic measurements are investigated. In addition, the impacts of these measurement errors on the estimation and study of the air–sea fluxes in the Gulf Stream are discussed. Pre- and postdeployment calibrations together with in situ comparison between shipboard and moored sensors supported the identification of biases due to sensor drifts, sensor electronics, and calibration errors. A postdeployment field study was used to further investigate the performance of the wind sensors. The use of redundant sensor sets not only supported the filling of data gaps but also allowed an examination of the contribution of random errors. Air–sea fluxes were also analyzed and computed from both Coupled Ocean–Atmosphere Response Experiment (COARE) bulk parameterization and using direct covariance measurements. The basic conclusion is that the surface buoy deployed in the Gulf Stream to support air–sea interaction research was successful, providing an improved 15-month record of surface meteorology, upper-ocean variability, and air–sea fluxes with known accuracies. At the same time, the coincident deployment of mean meteorological and turbulent flux sensors proved to be a successful strategy to certify the validity of the bulk formula fluxes over the midrange of wind speeds and to support further work to address the present shortcomings of the bulk formula methods at the low and high wind speeds.

1. Introduction

The large air–sea heat fluxes associated with warm western boundary currents imprint profound climate signatures on both the atmospheric and oceanic circulations (Minobe et al. 2008; Marshall et al. 2009). However, significant uncertainties about the magnitude and variability of these fluxes have persisted (Moore and Renfrew 2002). Renewed interest in improving the quantification of the air–sea coupling in western boundary current regions therefore triggered recent observational programs and campaigns in the northwest Pacific region (Kubota et al. 2008; Cronin et al. 2010; Konda et al. 2010). We discuss a recent effort to obtain accurate air–sea flux observations in the Gulf Stream region.

In the northwest Atlantic, past attempts to observe surface meteorology and air–sea interaction in the Gulf Stream region include the work done during the Genesis of Atlantic Lows Experiment (GALE) in January 1986 off the Carolinas. Bane and Osgood (1989) reported a heat loss of 1060 W m^{-2} during a cold-air outbreak over the Gulf Stream. In GALE the observations were made from existing weather buoys and additional buoys located on the continental shelf (Blanton et al. 1989); furthest offshore and nearest to the Gulf Stream, the sum of the latent and sensible heat fluxes was as high as 1400 W m^{-2} during a January cold-air outbreak. Yet,

Corresponding author address: Dr. Sébastien Bigorre, Woods Hole Oceanographic Institution, 266 Woods Hole Rd., MS 29, Woods Hole, MA 02543.
E-mail: sbigorre@whoi.edu

DOI: 10.1175/JTECH-D-12-00078.1

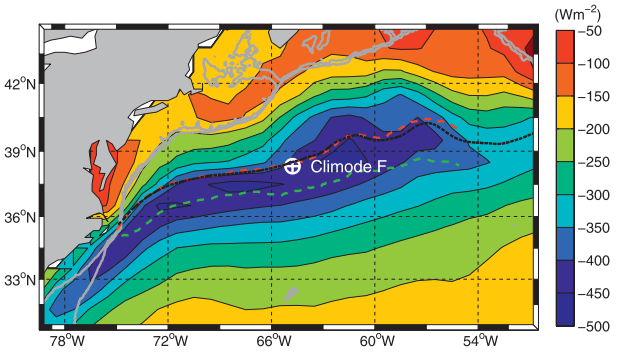

FIG. 1. Map of the Gulf Stream region, off the northeastern United States. The bottom bathymetry contours are shown in thick gray lines (200 and 1000 m). Color contours are the winter [December–March (DJFM)] mean net air–sea heat loss from sensible and latent heat from the objectively analyzed air–sea fluxes (OAFlux; Yu et al. 2004) for the winters of 2005–07. The average location of the north (south) wall of the Gulf Stream for the same period is indicated with the red (green) dashed line, based on the U.S. Navy front and eddy analysis product. The dashed black line is the average 18°C SST isotherm for the same period. The site chosen for the mooring, 38°N, 65°W, is shown by the white crossed circle.

significant uncertainties of the air–sea exchanges in deeper water remain, including over the core of the warm western boundary currents. Renfrew et al. (2002) found differences in the Labrador Sea between the mean turbulent heat fluxes (sensible plus latent) recorded on a research vessel over 40 days and those of the European Centre for Medium-Range Weather Forecasts (ECMWF) operational analyses and the National Centers for Environmental Prediction (NCEP) reanalyses of 38 and 130 W m^{-2}, respectively.

Winter buoyancy loss from the warm surface waters of the Gulf Stream has long been believed to be a key factor in the formation of the North Atlantic mode water known as 18°C Water (EDW). In 2005–07, the Climate Variability and Predictability (CLIVAR) Mode Water Dynamics Experiment (CLIMODE; Marshall et al. 2009) was conducted to investigate the various processes responsible for water mass transformation leading to EDW creation. Accurate air–sea measurements and turbulent fluxes collected near the Gulf Stream were therefore quite desirable, and we deployed a surface mooring during CLIMODE in the Gulf Stream region (Fig. 1). The surface mooring CLIMODE F was a 2.7-m-diameter foam hull buoy equipped with climate quality mean meteorological instrumentation (Weller and Anderson 1996) from which air–sea fluxes could be computed using the Coupled Ocean–Atmosphere Response Experiment (COARE) bulk formulas (Fairall et al. 1996, 2003). A direct covariance flux system (DCFS) also provided direct estimates of air–sea fluxes (Edson et al. 1998). With these two methods available, we hoped to evaluate the performance of the sensors as well as the bulk formulas. A companion paper (Weller et al. 2012) reviews the design of the surface mooring, the instruments deployed on the surface mooring, the sampling schemes used, and the data return from the 15-month CLIMODE F deployment; it also gives an overview of the collected data.

In this paper, we focus on quantifying the uncertainties associated with making these measurements in the challenging Gulf Stream regime. Section 2 describes the processing of the mean meteorological data, while section 3 discusses the direct covariance (DC) air–sea flux measurements. Section 4 focuses on the different biases that were identified in the data—in particular, in wind speed and direction—and then provides an analysis of the accuracy of the measurements. In section 5, the accuracies of air–sea fluxes are quantified and the bulk formulas and DCFS fluxes are compared. Finally, we conclude with section 6.

2. Processing of the mean meteorological data

We discuss here the processing of the data from the Air–Sea Interaction Meteorology (ASIMET) sensors deployed on CLIMODE F to collect mean meteorological data. For more details on these sensors, see Hosom et al. (1995) and Weller et al. (2012). Processing of the meteorological and oceanographic data records include linear correction for clock drift using pre- and postdeployment time marks in the records (e.g., plunging temperature sensors in an ice bath). All instruments were, where possible, calibrated before deployment and after recovery. Data from redundant sensors were compared with each other and also with measurements from ship during deployment and recovery operations. This allowed the identification of biases and drifts. Once each meteorological sensor record was corrected for known drifts and biases, data from redundant mean meteorological sensors were used to fill gaps and make one final set of mean meteorological time series (wind speed and direction, air temperature, barometric pressure, relative humidity, incoming shortwave radiation, incoming longwave radiation, and rain rate). To do this, a primary data record was first selected from the pool of redundant sensors, which had the least bias, the longest coverage, and the fewest anomalous data spikes. Gaps in this primary record were then filled by data from a secondary sensor. The criterion for accepting data from this secondary sensor was that the hourly moving average time series be within 5% of each other. When no secondary measurement was available to replace outliers or missing data in the primary record, a local time mean that excluded these data points was substituted. For all variables except wind speed, this local mean was an average

over 60 samples (1 h), and creation of 15-month time series for barometric pressure, incoming shortwave radiation, incoming longwave radiation, relative humidity, and air temperature was straightforward. Development of the precipitation and wind records required additional steps.

Raw precipitation data were noisy, and the rain rate was computed by first filtering the original accumulation data with a 20-min moving average and then time differencing and rejecting negative values higher than a nominal evaporation rate. The data were interpolated back to a 1-min sampling rate. ECMWF provided us with hourly time series of near-surface meteorological variables from their high-resolution forecast model output at the model grid point (38.46°N, 65°W), which was 25 (53) km northwest (north-northwest) of the mooring for the first (second)-year deployment. The rain gauge data compared well (in terms of rain events timing and intensity) with ECMWF high-resolution forecast model rain rates, and suspicious parts of the first year of in situ rain data (12 December 2005–31 January 2006 and 31 April 2006–19 November 2006) were replaced with the hourly ECMWF values linearly interpolated to 1-min resolution.

The ASIMET wind sensors were averaged and logged at 1-min resolution. The DCFS sensors were logged at 5 Hz for 20 min out of every hour (i.e., a one-third duty cycle); in the resulting 1-min average DCFS record, the first and last minutes were discarded because of end filter effects. Although the ASIMET wind sensors had multiple failures (in their vane, compass, and propellers), the instrument redundancy allowed for the construction of a continuous dataset until 12 September 2006, when Tropical Storm Florence damaged the propeller vane anemometers. From this date until the recovery in November 2006, the 1-min wind speed record comes from the DCFS system, linearly interpolated to 1 min for the full hour each hour. Comparison with ECMWF and Quick Scatterometer (QuikSCAT) data indicated the interpolation did not introduce any additional bias. The replacement criterion for suspicious or missing wind speed records was raised to 10%. The wind speed primary record was merged with the equivalent of 20 days of data from other sensors out of the 302 days of the first-year deployment that preceded the passage of Tropical Storm Florence. These substitutions did not change significantly the mean and variance of wind speed compared to the original primary record.

Wind direction measurement from the ASIMET sensors was also uncertain from the time of the collision with a ship (around 0800 UTC 19 January 2006) and subsequent repair (around 1600 UTC 12 April 2006). During this period, the only vane measurement available had a large offset and less variability compared to other periods. However, by correcting the offset using the DCFS wind data, the wind direction compared favorably with both DCFS and QuikSCAT. Although crude, this correction may be sufficient for low-frequency signals because the wind direction was the sum of the vane and compass measurements from the anemometer. As the buoy itself tended to be oriented facing the wind, the anemometer vane was mostly aligned with the buoy, such that most of the low-frequency variability was provided by the compass. The period with problematic vane signals corresponded to a time when the buoy was north of the Gulf Stream, when currents were weaker and the wind was therefore acting more efficiently on the buoy orientation. However, in infrequent cases with rapid variations in the wind direction, or weak wind speeds, the buoy may not have been facing the wind.

The resulting mean meteorological data were used together with the COARE version 3.0 bulk algorithm (Fairall et al. 1996, 2003) to compute bulk estimates of air–sea fluxes. To support computation of the fluxes, two Seabird 37 instruments on the buoy bridle at 0.89-m depth provided the ocean temperature closest to the sea surface, and the current velocity record at 10-m depth was used as the surface current estimate when computing the wind velocity relative to the sea surface.

3. Direct covariance air–sea fluxes

Air–sea fluxes were also estimated through DC measurements from the DCFS, which operated nearly continuously during the 15-month deployment. The sonic anemometer measures horizontal and vertical velocity components that are used to calculate turbulent velocity fluctuations after correction for platform motion. The covariance (or correlation) between the corrected vertical and horizontal velocity components provide the near-surface momentum flux or stress vector, given by

$$\boldsymbol{\tau} = -\overline{u'w'}\mathbf{i} - \overline{v'w'}\mathbf{j}, \tag{1}$$

where u', v', and w' are the along-wind, crosswind, and vertical velocity fluctuations, respectively; $\mathbf{i}$ and $\mathbf{j}$ are the along-wind and crosswind unit vectors, respectively; the overbar denotes the mean; and prime denotes the fluctuation about this mean. The instrument also measures the sonic temperature $T_s = T(1 + 0.51q)$, where T and q are the ambient temperature and specific humidity, respectively. This measurement closely approximates the virtual temperature $T_v = T(1 + 0.61q)$, and correlation with the vertical velocity provides an estimate of the buoyancy flux, given by

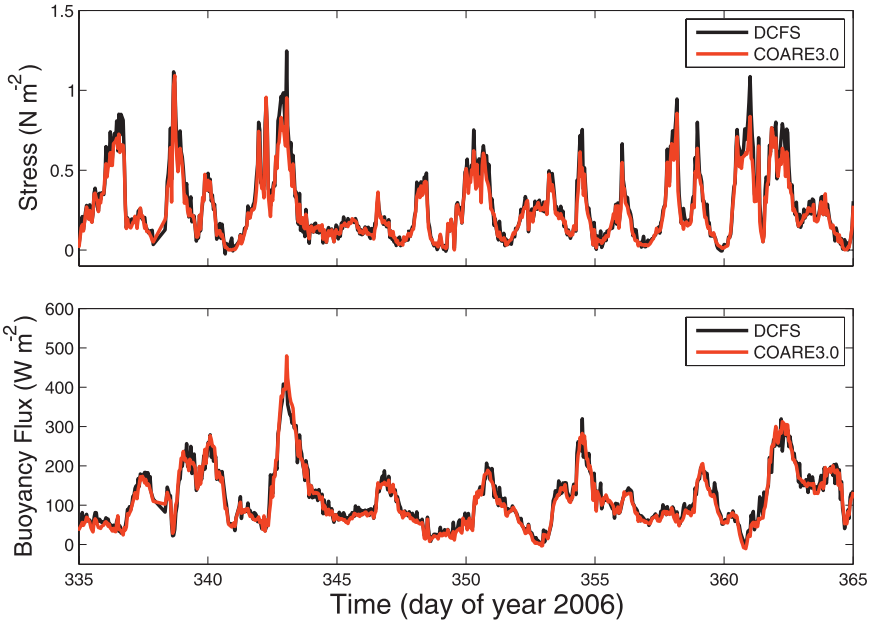

FIG. 2. Time series of DCFS and bulk fluxes of (top) momentum and (bottom) buoyancy for December 2006. The fluxes were derived from 20-min means computed every hour, i.e., the DCFS was operated on a one-third duty cycle. The DC fluxes are shown in black, and the COARE 3.0 fluxes are shown in red.

$$Q_B = \rho c_{\mathrm{pa}} \overline{w' T_v'} = Q_H(1 + 0.6\overline{q}) + Q_E 0.61 \frac{c_{\mathrm{pa}}}{L_e} \overline{T}, \qquad (2)$$

where Q_H and Q_E are the sensible and latent heat fluxes, respectively; ρ is the density of air; c_{pa} is the specific heat at constant pressure; and L_e is the latent heat of vaporization. The contribution of the sensible heat flux to the buoyancy flux is an order of magnitude larger than that of the latent heat flux when the magnitudes of these fluxes are roughly equivalent.

A comparison of the momentum and buoyancy fluxes estimates from the direct covariance method and bulk formula method using the COARE 3.0 algorithm is shown in Fig. 2. The buoyancy flux has been adjusted to account for the difference between the sonic and virtual temperatures using the latent heat fluxes from the COARE algorithm. The agreement between these flux estimates is overall very good. However, it was found that the bulk formula method underestimated the momentum flux and overestimated the buoyancy flux under high wind conditions. The findings are explained in more detail in section 5b.

4. Error analysis: Systematic biases

Errors in the meteorological mean variables have random and systematic components, the latter being generated, for example, by a bias or drift of the instrument. Other sources of uncertainty arise from environmental variability, sampling resolution, and methodologies used. For example, various atmospheric and oceanic forcing mechanisms tilt the buoy, which can decrease the response of propellers and enhance flow distortion. In this section, we focus on the biases that we could identify. During the deployment and recovery cruises, as R/V *Oceanus* was stationed for 24 h near the surface mooring, comparison of the shipboard and surface mooring measurements provided information on sensor performance. In addition, change between pre- and postdeployment calibrations provided a means to identify drift. However, several instruments were damaged during either the deployment or the recovery process. This limited the number of postrecovery calibrations. Finally, one field test of wind sensors was conducted after the CLIMODE field deployment, using sensors identical to the ones used during CLIMODE in order to confirm findings and solidify our conclusions.

a. Wind speed and direction

For wind measurements, no postcalibration was available and comparison between buoy and ship winds proved difficult, complicating the identification of biases. Wind speed estimates from the CLIMODE F buoy showed a discrepancy between ASIMET and DCFS measurements; the DCFS values tended to be larger. We found that the relative difference in wind speed between

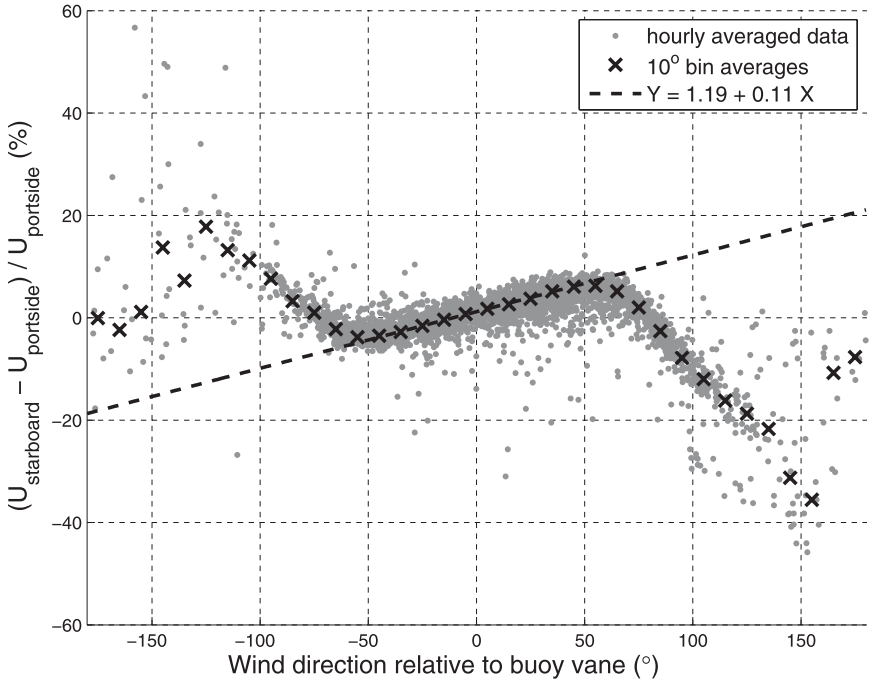

FIG. 3. Wind speed relative difference between two ASIMET propeller wind sensors as a function of wind direction relative to the buoy. ASIMET sensors are in opposite front corners of the buoy. Data are from a surface mooring in the South Pacific (Stratus Ocean Reference Station at 20°S) and based on 1 yr of data averaged hourly. Black crosses are bin averages from these data (10° bins) and the black dashed line is a linear fit for data with relative wind direction between −45° and 45°.

the two sensors was a function of wind direction relative to the buoy. This behavior has been seen in other deployments with similar buoy configuration and instrumentation; Fig. 3 shows the relative difference in wind speed between two identical ASIMET wind sensors (R. M. Young with vane and propellers) as a function of wind direction relative to the buoy. The data used in Fig. 3 are from a different deployment (subtropical South Pacific with very persistent southeasterly winds) that had no DCFS and no wind sensor in the center front location. The two R. M. Young sensors were placed on opposite corners of the buoy front. The linear dependence of the relative wind speed difference for wind directions relative to the buoy between ±50° is clear and repeatable across other similar deployments. The pattern is also almost perfectly antisymmetric with wind direction. Therefore, we hypothesize that our wind measurements from surface moorings are subject to wind flow distortion, which leads to a bias of up to 5% in wind speed. Note that the incoming wind can be oblique with respect to the buoy because the action of the buoy vane, which tends to align the buoy into the wind, is counteracted by a torque created by the wind on the asymmetric structure of the buoy's central well that hosts the batteries and electronics. Because of these two opposite forces, the buoy actually tends to orient at about ±(20°–30°) from the incoming wind.

In Fig. 4, we show a top-view schematic of wind instrumentation on CLIMODE F. For more details of the buoy and its instrumentation, see Weller et al. (2012, their Fig. 2). Our interpretation of the relative wind-direction-dependent bias in wind speed is also illustrated in this figure. In the situation depicted, the wind impinges on the buoy with an angle of about 30°, interacting first with the front port-side corner of the buoy. We hypothesize that the tower on the buoy deflects the airflow, creating a divergence near the stagnation point in the front port-side corner. The wind sensor nearest to the divergent flow may therefore measure a low biased wind speed. Similar to Fig. 3, data from CLIMODE F are shown in Fig. 5, where the wind heading on the graph's x axis is relative to the buoy vane, positive counterclockwise. The data were first organized in 5° bins from which the mean and standard deviation were extracted and plotted. The wind speed relative difference is also systematically computed between the DCFS on the starboard side of the buoy and one ASIMET wind sensor farther on the port side (one in the center, the

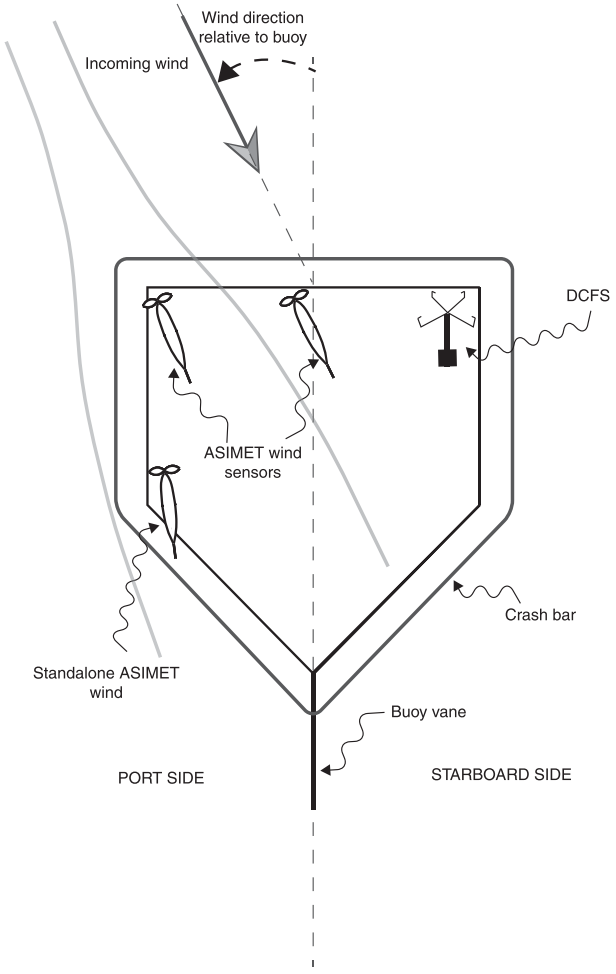

FIG. 4. Top-view schematic of CLIMODE F surface mooring. Only wind sensors are portrayed for simplicity. The incoming wind tends to have an angle with the buoy front, due to asymmetry of the buoy well. In the situation portrayed here, the wind comes from the port side of the buoy. The thick gray lines are a hypothetical representation of the streamlines that encounter obstacles like the crash bar or wind tower [for more details of the buoy and its instrumentation, see Weller et al. (2012, their Fig. 2)]. Wind sensors are located above this, but may still be influenced by some of the distorted streamlines.

other on the port-side front corner). We focus here on winds that are within 50° of the buoy (0° being aligned with the buoy vane), because this is where most data exist. As the incoming wind moves from starboard (negative abscissa) to port side (positive abscissa), the wind speed relative difference (DCFS minus ASIMET) increases. The measurements shown here and CFD simulations (Edmond et al. 2012) indicate that flow distortion can create up to a 5% wind speed difference between sensors on different sides of the buoy. The differences exhibited during CLIMODE were larger—up to 10% between DCFS and ASIMET—so further error sources were sought.

We began by investigating the effect of vertical components of the wind on the different sensors. The DCFS measures wind along three orthogonal axes, which can be used to measure the total tilt in the sonic reference frame. This tilt is due to a combination of physical tilting of the anemometer–platform relative to vertical and tilting of the flow due to flow distortion. In principle, the platform tilt is removed and the DCFS wind components are rotated into a level reference frame after motion correction. Any tilt remaining after motion correction is mainly due to flow distortion by the superstructure. Therefore, the difference between the total tilt measured by the sonic and the platform tilt measured by the motion sensors represents the tilt in the flow due to flow distortion.

Bin-averaged estimates of the total (squares and lines), platform (line), and remaining (circles and lines) tilt are shown in Fig. 6. The platform tilt is well represented by 5° pitching up of the buoy as modeled by the broken line in Fig. 6. This was confirmed by measurements, which showed a mean pitch of approximately 4.85° ±1.88° and a smaller roll of 0.55° ±0.75°. The pitch was linearly dependent on wind speed ranging from approximately 3° at low winds to 8° at high winds. Therefore, the mean pitch is likely due to a combination of drag on the buoy and mooring by winds, waves, and currents, along with a simple weight imbalance of the sensor packages, battery packs, and other structures on the buoy.

The tilt that remains after motion correction is positive for all relative wind directions. This is due to airflow distortion from the buoy structure, which deflects the incoming wind upward. For winds coming from the starboard side (negative abscissa in Fig. 6), the tilt of the wind at the DCFS location peaks, with values between 5° and 6°. As the incoming wind rotates counterclockwise, the tilt measured at the DCFS location decreases to approximately 3° for incoming wind coming from the port side of the buoy (positive abscissa). As shown in the bottom panel of Fig. 5, the majority of the relative winds (~80%) are between ±40°; whereas the motion-corrected tilts are between 4° and 5°. Contrary to the DCFS, the R. M. Young propeller–vane sensor can measure only 2D wind. Its response function is close to cosine for small values of the wind angle with its propeller axis (less than 30°). Assuming the ASIMET sensor samples only the horizontal wind in a framework similar to the DCFS, it should therefore also underestimate the true horizontal wind component. To quantify this we first compute a linear regression of the horizontal wind (U^h) measured by the DCFS in the tilted frame against the horizontal wind speed computed in the level frame. This is given by

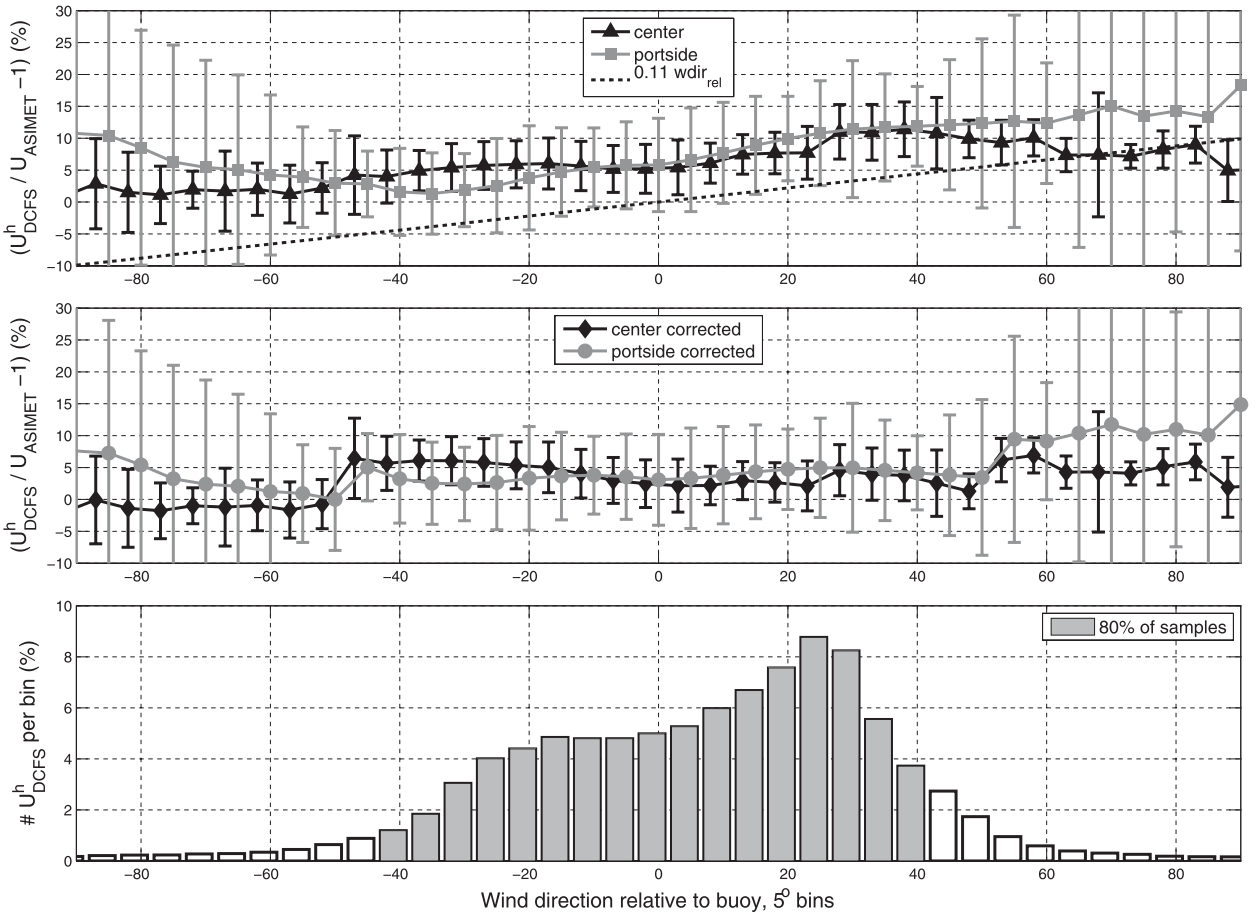

FIG. 5. (top) Wind speed relative difference (%) between DCFS and ASIMET sensors as a function of wind direction relative to buoy vane (positive counterclockwise). The DCFS was on the buoy front starboard side. One ASIMET was on front center and the other on front port side. Lines and symbols represent the mean values from 16-min-averaged data in 5° bins; error bars are the standard deviations about these means. (middle) As in (top), but ASIMET wind speed is corrected for lateral distortion and vertical tilt, using Eq. (4). (bottom) Distribution of wind speed with respect to wind direction relative to the buoy.

$$U^h_{\mathrm{DCFS}_{\mathrm{level}}} = -0.1 + 1.04 U^h_{\mathrm{DCFS}_{\mathrm{tilted}}}. \quad (3)$$

We then assume the ASIMET horizontal wind speed also underestimates the true horizontal wind speed by the same 1.04 multiplying factor. Combining this correction with the lateral distortion shown in Fig. 3, we can write, using $\langle\cdot\rangle$ notation for 1-min averages,

$$\left\langle U_{\mathrm{ASIMET}} \right\rangle \cong \left\langle U^h_{\mathrm{DCFS}_{\mathrm{level}}} \right\rangle \left(1 - \frac{0.11}{100}\mathrm{wdir}\right)/1.04. \quad (4)$$

Equation (4) is used to correct the ASIMET wind speed record, which decreases the relative difference with DCFS from 10% to about 5%, as seen in Figs. 5 and 7. The histogram in the bottom panel of Fig. 7 indicates that a 5% difference is reachable for most situations.

In these comparisons, the wind speed data are adjusted to the height of the DCFS sensor using the COARE 3 algorithm. However, compared to the DCFS, the vertical flow is higher near the ASIMET sensors, which are lower and therefore closer to the top of the buoy tower. There is an indication from CFD simulations (Edmond et al. 2012) that the streamlines intersecting the ASIMET wind sensors originate about one foot lower upstream of the buoy, whereas the deflection at the DCFS location is much lower. Assuming the ASIMET samples airflow that is in fact 0.3 m lower, the height adjustment to DCFS should increase ASIMET wind speed values by only about 0.8%.

Which wind speed is closest to the true wind, away from the buoy-distorted wind flow? We attempted to answer this question with a short buoy deployment near the Martha's Vineyard Coastal Observatory (MVCO) Air-Sea Interaction Tower (ASIT) in about 15 m of water off the island in late spring of 2010. The buoy was similar in configuration to the second deployment of

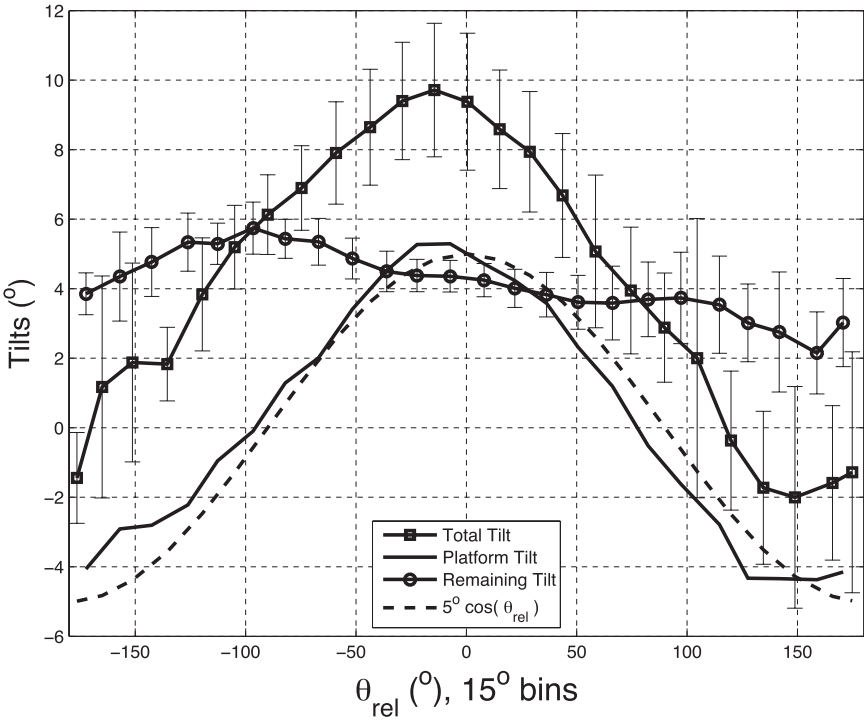

FIG. 6. DCFS wind vertical tilt (degrees) vs relative wind direction (where 0° is head on) using 18-min averages. The lines represent the total tilt, platform tilt, and remaining vertical tilt after rotation into the local vertical frame of reference as labeled. The remaining tilt is assumed to be a result of flow distortion. The symbols represent the means computed in 15° relative wind direction bins, and the error bars are the standard deviations about these means.

CLIMODE F (e.g., ASIMET wind sensors consisted of one 2D sonic in the center front and one vane propeller in the port side front corner of the buoy tower) and was located 500 m upwind of the ASIT. The observed wind speeds were smaller than during CLIMODE, and the buoy motion was also reduced. With less instrumentation on the buoy superstructure, flow distortion may also have been reduced compared to CLIMODE. The buoy orientation stayed mostly about 30° to the right of the wind, so we cannot make the same comparisons we did for CLIMODE because we do not have the same range of relative wind directions. Wind direction on the buoy was on average about 5° off the ASIT estimate but this bias is not significant since the accuracy of the compasses is also about 5°. As for wind speed, in the range observed during CLIMODE MV (0 to 14 m s^{-1}), estimates from ASIT are slightly lower than the buoy DCFS (2%) which itself is higher than the ASIMET buoy propeller vane (5%) and 2D sonic (1%). These differences are quite small (i.e., never exceeding 5%) and comparable to the sensors' accuracies. It is therefore reassuring that wind speed measurements on the buoy are reasonably close to the real wind, at least in the speed range mentioned above.

Flow distortion is believed to be the major source of error in wind speed. Our observations show that up to 5% relative error in wind speed can exist between two identical sensors, with the low biased sensor being closer to the zone where the incoming airflow first impinges on the buoy structure. This result is qualitatively and quantitatively consistent with computational fluid dynamics (CFD) simulations (Edmond et al. 2012) that also show that at the location of the low biased instrument, the 3D wind speed is similar to the undisturbed airflow but that the horizontal component is slightly lower. Vertical tilt of airflow, partly due to buoy tilt and to vertical airflow distortion, tends to produce underestimates of wind speed when measured by 2D wind sensors like the ASIMET ones used here. This low bias compensates in part for the lateral acceleration. Therefore, we think that ASIMET wind speeds presented in this work are 0%–5% lower than the undisturbed wind speed. For high wind speeds, the low bias in the 2D wind from ASIMET may increase. The motion-corrected DCFS wind speed measurement is probably closer to the true wind, although it may have a small high bias. We saw that an empirical correction, dependent on wind speed and wind direction relative to the buoy,

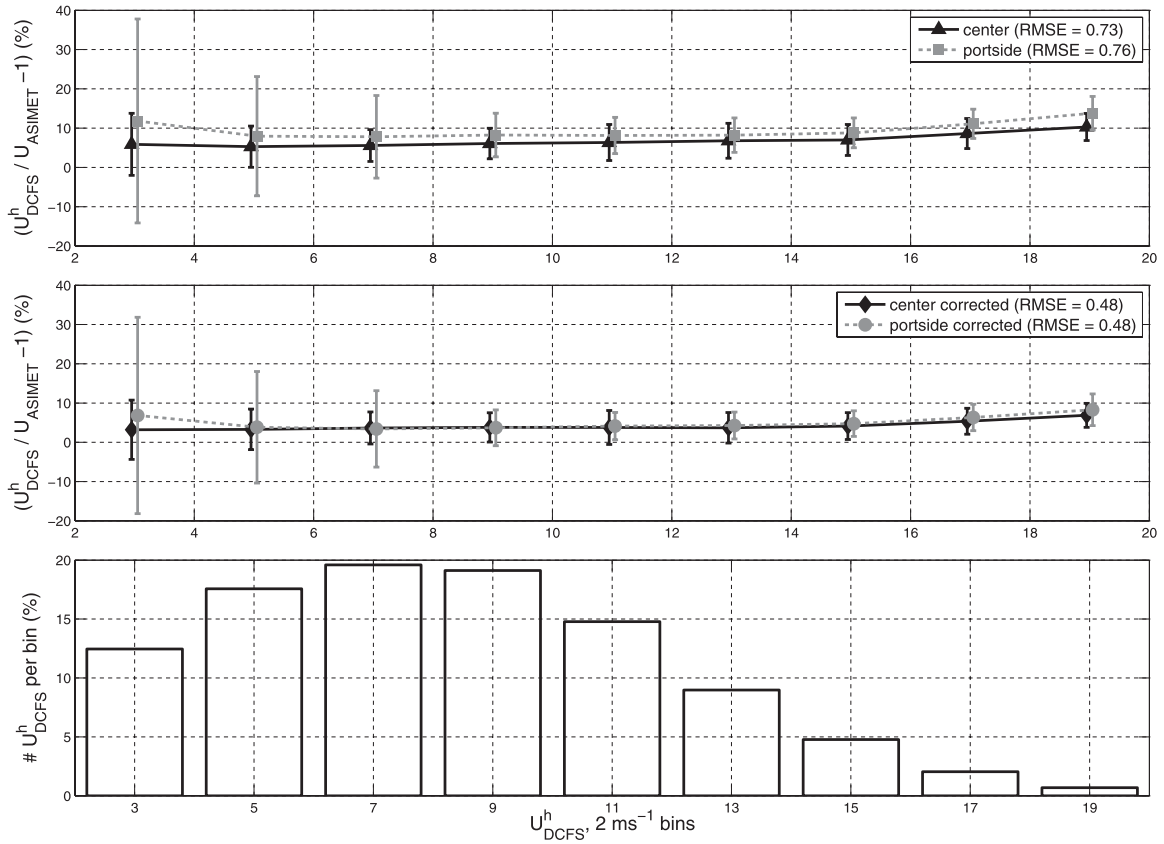

FIG. 7. Relative wind speed difference between DCFS (horizontal component in level reference frame) and ASIMET, based on 16-min-averaged data as a function of wind speed. One ASIMET was in the center front, and the other was in a port-side front corner of the buoy. The DCFS was in the front starboard corner. (top) Raw data. (middle) ASIMET corrected [Eq. (4)] for lateral distortion and vertical tilt. (bottom) Histogram of the relative wind speed difference with respect to wind speed.

could be used to adjust the 2D ASIMET wind speed closer to the DCFS value and therefore the undisturbed wind. To be conservative, our error is therefore less than 5% for winds less than 15 m s^{-1} and below 10% for stronger winds (Fig. 7). A 10% error for the whole wind speed range is probably a worst-case scenario.

b. Other meteorological data

Based on comparisons between shipboard and surface mooring measurements during the recovery cruise, as well as postrecovery calibrations, we identified end-of-deployment offsets in some of the ASIMET data. Experience suggests ASIMET sensors drift linearly with time. We therefore applied an empirical linear drift that matched the final offsets. Colbo and Weller (2009) discuss in detail the errors that are typical in ASIMET measurements, although in less dynamic environmental conditions (subtropics).

We estimated a dry linear drift in relative humidity (RH) of -0.0026% day^{-1} and cold-air temperature drift of -3.4×10^{-4} °C day^{-1}. After a year, these drifts would induce offsets of -0.96% and -0.12°C, respectively. Barometric pressure had a drift of 2.97×10^{-4} hPa day^{-1}. Small offsets in the incoming longwave radiation sensors were encountered that were caused by instabilities of the thermopile voltage amplifier. Based on cross-sensor comparison, we estimated the typical error from this source to be within 8 W m^{-2}, with slightly higher values in the winter. In our final dataset, incoming longwave radiation values were increased by 15.18 W m^{-2} to agree with R/V *Oceanus* measurements at recovery and for consistency with postdeployment calibrations. As we saw earlier, the buoy and therefore the radiometers were tilted, which induces discrepancies with the amount of radiated energy compared to a horizontal surface. The in situ measurement of precipitation is underestimated because of the undercatch of falling raindrops caused by flow distortion above the rain gauge. The undercatch depends strongly on wind speed but also possibly on rain rate or drop size. For daily values, estimates of 20% undercatch have been proposed (Yang et al. 1998; Serra et al. 2001; Serra and

TABLE 1. Measurement errors for 1-min data to daily averages. Cross-sensor error is defined as one standard deviation of the difference between two records from duplicate sensors. Systematic biases arise from drift correction, calibration, or environmental conditions. Drift values correspond to observed offset at postcruise calibration, after 1-yr deployment.

Bulk measurement	Cross sensor standard deviation				Systematic biases
	Instantaneous	10 min	Hourly	Daily	
Incoming longwave (W m^{-2})	5	3.9	3.6	3.1	Tilt: unknown (<5%) Amplification bias: <15
Incoming shortwave (W m^{-2})*	17	7.1	5	1.5	Tilt: <5%; calibration low bias: <5%
RH (% RH)	2.3 (2.7 winds > 6 m s^{-1}) (1.7 winds < 6 m s^{-1})	1.7	1.3	0.6	Drift: 1
Air temperature (°C)	0.3	0.25	0.2	0.12	Drift: 0.1
Wind speed (m s^{-1})	0.7	0.25	0.22	0.16	Drift: 0.1; flow distortion: 5% Tilt: 5%
Wind direction (°)**	7.5	2.6	1.8	1.5	Accuracy and flow distortion: <10
Bulk SST (°C)	0.025	$8.4\ 10^{-3}$	0.004	$8\ 10^{-4}$	Flow distortion: small, maybe high bias
Barometric pressure (hPa)	0.32	0.15	0.12	0.083	Drift: 0.11
Rain rate (mm h^{-1})	Large due to low-pass filtering		~20%	20%	Low bias increases with wind speed

* Incoming SWR estimates based on daylight data.
** Wind direction data for the period 19 Jan 2006–12 Apr 2006 should be taken with caution and have a higher uncertainty.

McPhaden 2003). Our data indicate that many observed rain events also corresponded to periods of high winds (warm and cold fronts ahead of low pressure atmospheric systems) and were short lived (less than a few hours), so that undercatch may be even more pronounced on these short time scales. Table 1 reviews some of these biases.

The bulk SST measured under the buoy may actually be more characteristic of water parcels closer to the air–sea interface, because of the downward deflection of the flow past the buoy hull. Thus, a high bias may exist in our SST measurement, but it is most probably very small due to the sustained high winds observed in the Gulf Stream region. Similarly, the cool skin correction was not directly measured during CLIMODE, but the parameterization included in the COARE 3 algorithm gave estimates with values up to 0.7°C during high heat loss events in winter. Similarly, we expect the current measurement at 10-m depth to be different from the actual interface value. Using the DCFS motion package, estimates of significant wave height were obtained that were linearly related to wind speed ($H_{sig} = 0.18U_{air}$). This linear fit is quite close to a Joint North Sea Wave Project (JONSWAP[1]) estimate with 125-km wind fetch (not shown). Given that at 10-m depth, wind wave orbital velocities decrease at a rate of 0.5 m s^{-1} per meter of wave amplitude (half the wave height), we infer that surface velocities may be $0.045U_{air}$ higher than the measured value from the current meter.

c. Subsurface data

The main source of biases in the subsurface temperature data stems from the tilt of the mooring line, which makes the actual depths of the sensors shallower than their nominal depth (distance along the mooring line). Strong currents and drag on the mooring line and instruments caused this tilt. The two Nortek Aquadopp acoustic Doppler current meters recorded current velocities at 10- and 20-m depths, as well as instrument tilts. Current speeds measured at both depths were nearly identical. The deepest sensor on the mooring line was a Seabird 37, which also recorded pressure and allowed the computation of its actual depth, denoted as z_{bottom}. Its nominal depth was 662 m, but z_{bottom} ranged from 663.7 to 550.7 m with a mean of 644.5 m. Assuming the mooring line was straight above this lowermost sensor, an estimate of the tilt would be $\Theta_{z=662} = \cos^{-1}(z_{bottom}/662)$. Tilt measured at 20 m was less than 10° for 82% of the deployment duration. All three tilts mentioned above were clearly dependent on the current speed and the following linear regressions were obtained: $\Theta_{z=10} = -0.2 + 5.9U_{current}$ (with RMSE = 1.7°), $\Theta_{z=20} = -0.3 + 8.3U_{current}$ (with RMSE = 2°), and $\Theta_{z=662} = -0.13 + 14.7U_{current}$ (with RMSE = 2.6°), where $U_{current}$ denotes current speed (in m s^{-1}) measured by the Aquadopps and the tilts (θ) are in degrees. These tilt estimates and their increase with current speed and depth are in very good agreement with numerical simulations of the mooring line shape, using the Cable software (Gobat and Grosenbaugh 2000), and they indicate the mooring line was not really straight

[1] JONSWAP refers to the wave spectrum defined by Hasselmann et al. (1976) and is based on in situ data from JONSWAP. JONSWAP takes into account nonlinear interactions between waves, thus extending the wave spectrum to growing sea conditions. The spectrum leads to a wave significant height given by $H_{sig} = 4\sigma_H$ and $(\sigma_H)^2 = 1.67 \times 10^{-7}(xU_{10})^2/g$, where x is fetch and U_{10} is wind speed at 10-m height.

but rather sagged downward. However, we assumed a straight mooring line and applied a linear depth correction to all 18 subsurface temperature sensors by multiplying their nominal depths with $R = z_{\text{bottom}}/662$ at each time step. The correction factor R used here, which is depth invariant, is therefore high biased near the surface and slightly low biased near 662-m depth. Near the surface, the high bias can reach up to 10° or 15°, whereas in the lower 300 m the low bias is less than 5°. The error in estimated depth is $\Delta z \cong z\sin(\Theta)\Delta(\Theta)\pi/180$, where z is nominal depth, Θ is mooring line tilt, and $\Delta(\Theta)$ is the tilt error. Near the surface, assuming $\Theta \sim \Delta(\Theta) \sim 15°$, $z \sim 20$ m leads to $\Delta(z) \sim 1.3$ m. Lower in the water column, this error could be larger as z increases and tilts remain large, but it is less than the vertical resolution of the sensor array.

d. Random errors

The random errors in our measurements were estimated using the difference between measurements from redundant sensors, $\Delta X = \text{X1} - \text{X2}$, where X1 and X2 were the redundant measurements of the same meteorological variable X, after drift correction. We used the first 6 weeks of data available for most of our variables because some sensors failed after that period and also to limit the influence of possible residual drifts and to remain close to the predeployment calibrations. Time series of ΔX averaged over 10 min were used to construct normalized histograms (Fig. 8). The average (μ_X) and standard deviation (σ_X) of ΔX were also calculated. The number of underlying data points reached nearly 5000 or more (incoming shortwave radiation had less, since only daylight periods were used). For wind direction, which is a circular variable, μ_X and σ_X were computed using Yamartino (1984). Most observed probability density functions (PDFs) have a narrower spread than the normal distributions $N(\mu_X, \sigma_X^2)$. Remaining biases can be identified in these histograms as the mean value or dominant mode and are relatively small. Table 1 summarizes values of σ_X for different averaging intervals, thus providing estimates of the measurement errors. The relative error of the 10-min averaged data is within 5% for most of the variables. It is less than 2% for incoming longwave radiation and below 0.1% for sea surface temperature and barometric pressure. Wind speed and shortwave radiation had large instantaneous errors because these variables are highly variable from one minute to the next, which combined with small differences in instruments clocks can lead to large measurement differences. For these two measurements, the cross-sensor standard deviation drops quickly as data samples are averaged together. At low values, these two measurements also exhibit large relative variations. For winds less than 6 m s^{-1}, this relative error can go up to 10% and beyond for very low winds.

As samples are averaged together, the central limit theorem predicts that the standard deviation of the averaged data $\overline{\sigma}$ decreases like $1/\sqrt{N}$, with N being the number of samples forming the average. For correlated random variables, N should be replaced with the effective number of observations N_{eff} (Zhang 2006; Zięba 2010), written as

$$\overline{\sigma}^2 = \left[1 + \frac{2\sum_{i=1}^{N-1}(N-i)\hat{\rho}(i)}{N}\right]\frac{\sigma^2}{N} = \frac{\sigma^2}{N_{\text{eff}}}, \tag{5}$$

where σ and $\rho(i)$ are the standard deviation and autocorrelation at time lag i of the original 1-min time series ΔX, respectively. Figure 9 shows how $\overline{\sigma}$ decreases asymptotically as $\sigma/\sqrt{N_{\text{eff}}}$ for large samples. In contrast, for small N, the formula for N_{eff} is inaccurate (Zhang 2006). We can use Fig. 9 to quantify the random error of our measurements in Table 1. Note that bulk variables are often averaged hourly before they are used in bulk formulas to compute the fluxes.

5. Air–sea flux accuracies

The impacts of the observational errors and uncertainties on the computation of the air–sea fluxes are examined here.

a. Errors in bulk flux estimates

The COARE bulk algorithm is based on the Monin–Obukhov layer theory, which assumes that turbulent fluxes are constant near the surface. In reality, fluxes vary by approximately 10%, which is commensurate with the uncertainty of measurements, so the assumption is valid (Shaw 1990). In this section we describe the uncertainties in air–sea flux estimates from bulk parameterization. The following equations are the bulk flux estimates:

$$Q_H = \rho c_{\text{pa}} C_H S(\overline{T}_s - \overline{\theta}), \tag{6}$$

$$Q_E = \rho L_e C_E S(\overline{q}_s - \overline{q}), \tag{7}$$

$$\tau = |\boldsymbol{\tau}| = \rho C_D S(\overline{u}_s - \overline{u}), \tag{8}$$

where C_H, C_E, and C_D are the bulk transfer coefficients for heat, mass, and momentum, known as the Stanton number, Dalton number, and drag coefficient, respectively; S is the magnitude of the wind speed relative to water, $\overline{\theta}$ represents the mean potential temperature, $\overline{u}_s$ is the component of the mean current in the direction of

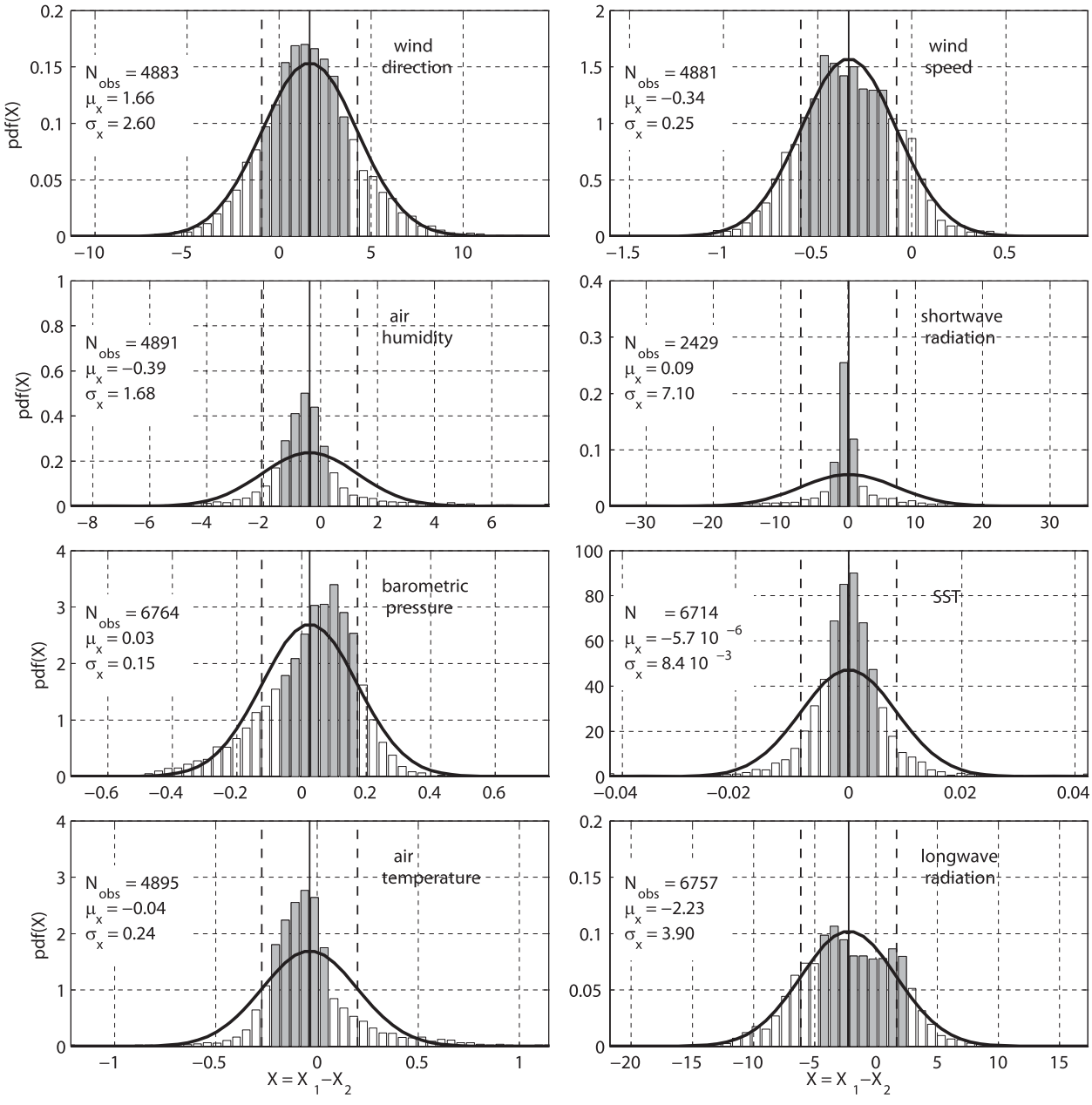

FIG. 8. Errors in bulk variable measurements. (top to bottom) (left)Wind direction (degrees), air RH (%), barometric pressure (hPa), air temperature (°C); (right) wind speed (m s^{-1}), SWR (W m^{-2}), sea surface temperature (°C), and LWR (W m^{-2}). Bars indicate histograms of differences in measurements from two primary sensors, $X = X_1 - X_2$ based on 10-min averages of original 1-min data. Here, the y axis represents the proportion of values that are inside each bin on the x axis. Number of observations for X, average, and standard deviation are included as text. Equivalent Gaussian distribution (same mean and standard deviation) shown as black curve. Mean difference also shown as the vertical black line. Dashed vertical lines are the one standard deviation lines of the equivalent Gaussian. Gray bins are the 68th percentile of the data PDFs.

the wind, and $\overline{u}$ is the vector-averaged wind. Also, T_S and q_S are the temperature and specific humidity of air parcels near the water interface, respectively; therefore, T_S is equivalent to the skin sea surface temperature (SST) and q_S is the saturated specific humidity at temperature T_S. Note that above the ocean, q_S is reduced by 2% from its value above pure water at temperature T_S to account for the salinity effect on vapor pressure (Fairall et al. 1996).

The bulk transfer coefficients in Eqs. (6)–(8) are based on experimental fits and therefore have uncertainties. Fairall et al. (2003) discuss the COARE 3.0 bulk

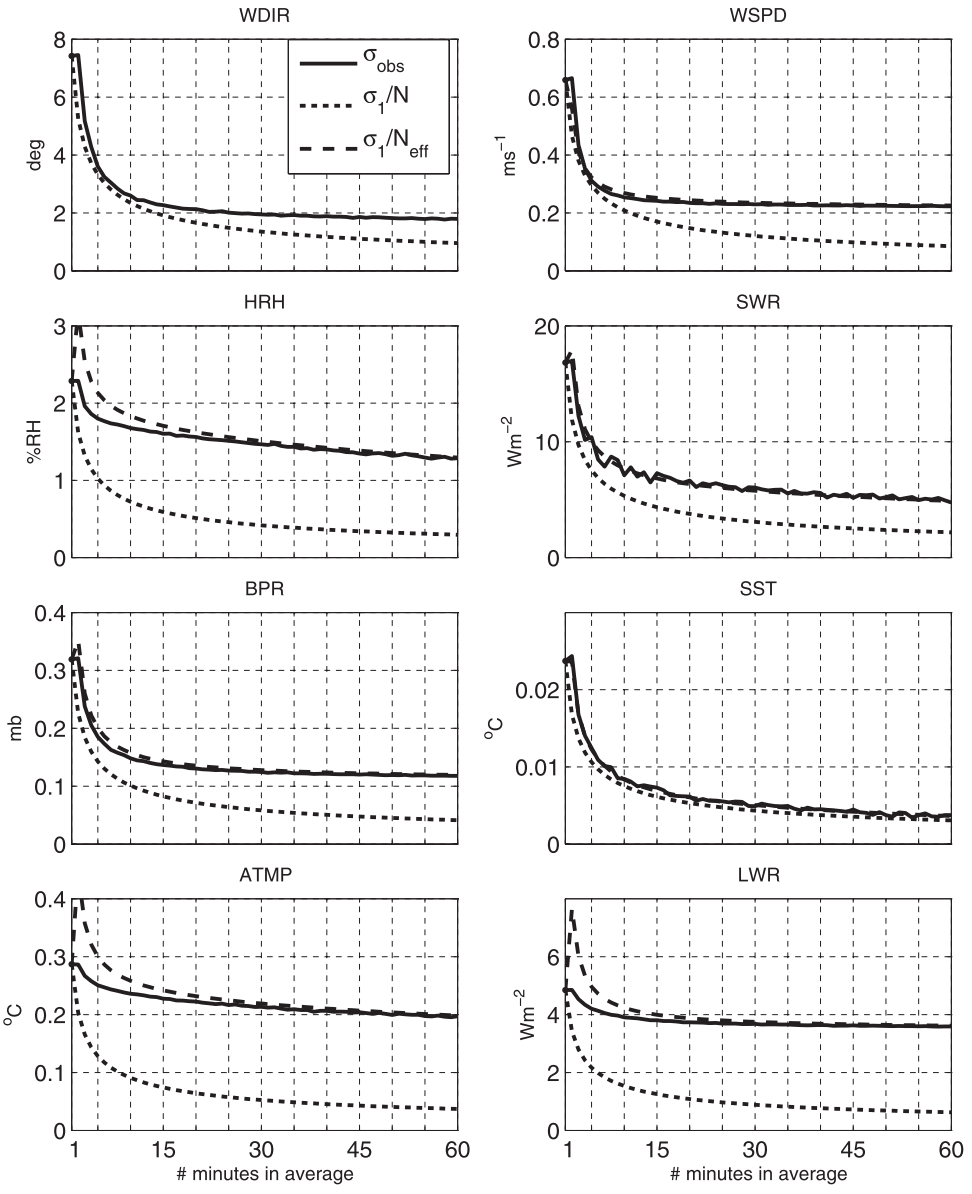

FIG. 9. Standard deviation of difference between two ASIMET measurements for each bulk variable (panels ordered as in Fig. 8), as a function of number (N) of samples averaged together: data (solid lines), $\sigma_{N=1}/\sqrt{N}$ (dotted lines), and $\sigma_{N=1}/\sqrt{N_{\text{eff}}}$ (dashed lines).

algorithm and state that the transfer coefficients have a root-mean-square (RMS) error of 5% for winds below 10 m s^{-1} and less than 10% for winds between 10 and 20 m s^{-1}. These and the measurement uncertainties of the bulk variables propagate through the bulk formulas as shown by Colbo and Weller (2009), which we reproduce here. The relative error or uncertainty in the sensible heat flux is estimated from

$$\left(\frac{\partial Q_H}{Q_H}\right)^2 = \left(\frac{\partial C_H}{C_H}\right)^2 + \left(\frac{\partial S}{S}\right)^2 + \frac{\partial\overline{\theta}^2 + \partial\overline{T}_s^2}{(\overline{\theta} - \overline{T}_s)^2}. \tag{9}$$

Similarly, the relative error in latent heat flux is estimated from

$$\left(\frac{\partial Q_E}{Q_E}\right)^2 = \left(\frac{\partial C_E}{C_E}\right)^2 + \left(\frac{\partial S}{S}\right)^2 + \frac{\partial\overline{q}^2 + 0.96\partial\overline{q}_s^2}{(\overline{q} - 0.98\overline{q}_s)^2}. \tag{10}$$

However, the specific humidity, as measured on the buoy, is a function of temperature, pressure, and relative humidity, written as

$$\overline{q} \cong \text{RH} \times q_{\text{sat}}(\overline{T}, \overline{p}), \tag{11}$$

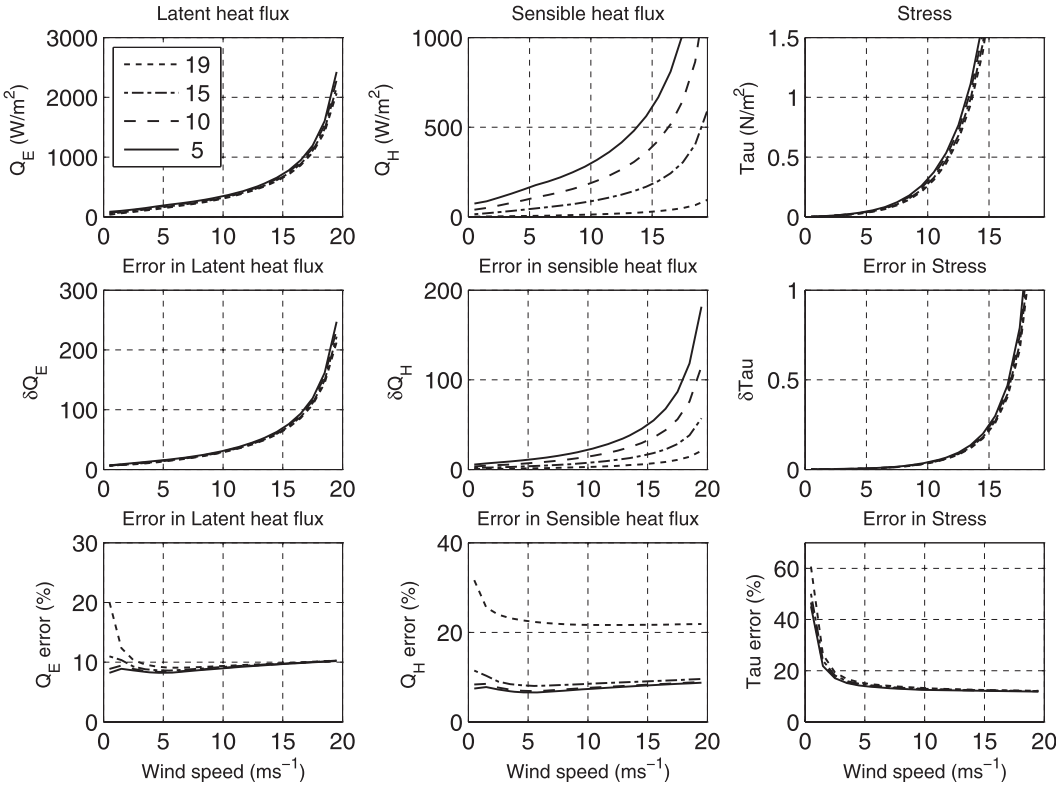

FIG. 10. Air–sea heat fluxes and their errors, estimated from COARE 3.0, as functions of wind speed (x axis) and air temperature T_{air} (line styles, see legend in top-left plot) and with SST fixed at 20°C and air-specific humidity 6 g kg^{-1}; these conditions were common in winter. (left) Latent heat, (middle) sensible heat, and (right) momentum fluxes. (top) Flux values, (middle) absolute error, and (bottom) relative error.

where RH is the relative humidity (in %) and q_{sat} represents the saturation specific humidity at the ambient temperature and pressure. Therefore, the relative error in the latent heat flux can be written

$$\left(\frac{\partial Q_E}{Q_E}\right)^2 = \left(\frac{\partial C_E}{C_E}\right)^2 + \left(\frac{\partial S}{S}\right)^2 + \frac{\mathrm{RH}^2 \partial q_{\text{sat}}^2 + q_{\text{sat}}^2 \partial \mathrm{RH}^2 + 0.96 \partial \overline{q}_s^2}{(\mathrm{RH} q_{\text{sat}} - 0.98 \overline{q}_s)^2}. \quad (12)$$

The momentum stress error is

$$\left(\frac{\partial \tau}{\tau}\right)^2 = \frac{\partial C_D^2}{C_D^2} + 4\frac{\partial U^2 + \partial U_s^2}{(U - U_s)^2}, \quad (13)$$

where $S = U - U_s$. Finally, the errors in the net longwave and shortwave radiation fluxes are as in Colbo and Weller (2009) as shown:

$$\partial Q_{\text{LW}}^2 = \varepsilon^2 \partial \downarrow Q_{\text{LW}}^2 + 16 \varepsilon^2 \sigma_{\text{SB}}^2 \overline{T}_S^6 \partial \overline{T}_S^2, \quad (14)$$

$$\partial Q_{\text{SW}}^2 = \downarrow Q_{\text{SW}}^2 \partial \alpha^2 + (1 - \alpha)^2 \partial \downarrow Q_{\text{SW}}^2, \quad (15)$$

where $\downarrow Q_{\text{LW}}$ and $\downarrow Q_{\text{SW}}$ represent the downwelling (i.e., measured) components of the longwave and shortwave radiative fluxes, respectively; ε is emissivity; σ_{SB} is the Stefan–Boltzmann constant; and α is albedo.

Uncertainties of the hourly averaged bulk variables presented in the previous section (Table 1) were propagated in the COARE algorithm (Bradley and Fairall 2006). Assuming a 5% relative error in all transfer coefficients, the resulting uncertainties in bulk air–sea fluxes are shown in Fig. 10. The wind speed uncertainty was modeled as an offset (0.2 m s^{-1}) and gain (6%), in keeping with the difference between ASIMET and the DCFS measurements corrected for platform motion. Air temperature and humidity uncertainties were modeled as 0.2°C and 0.4 g kg^{-1} offsets, respectively. SST and air specific humidity were kept constant at 20°C and 6 g kg^{-1}, respectively, while air temperature ranged from 5° to 19°C, similar to observations during CLIMODE. Our choice of SST is important since it directly influences q_s and therefore the vertical gradient in q. For a higher SST value, the latent heat flux would rise and the associated relative error would decrease. After

TABLE 2. Absolute errors in air–sea differences of temperature, humidity, wind speed, and resulting relative errors in latent (Q_E), sensible (Q_H), and momentum bulk fluxes using COARE 3.0. Relative errors (%) of air–sea bulk fluxes, using propagation of random errors in Table 1 through COARE 3.0 algorithm. Relative errors in fluxes are median values of CLIMODE time series for the different sample averaging periods in each column (these errors are high biased due to small heat loss events, usually in summer).

Variable	10 min	Hourly	Daily
$\Delta(T_{sea} - T_{air})$ (°C)	0.25	0.2	0.15
$\Delta(q_{sea} - q_{air})$ (g kg^{-1})	0.5	0.4	0.35
$\Delta(U_{sea} - U_{air})$ (m s^{-1})	$0.35 + 0.06U_{air}$	$0.2 + 0.06U_{air}$	$0.2 + 0.06U_{air}$
$\Delta Q_E/Q_E$ (%)	13.6	11.2	10.2
$\Delta Q_E/Q_E$ (%)	14	11.4	10.1
$\Delta\tau/\tau$ (%)	15.8	13.8	13.8

trying different combinations of values for the bulk variables, it appears the worst error in the latent heat flux reaches 20% for low wind and near-neutral stability conditions. Relative errors in sensible heat and momentum fluxes are below 10% and 15%, respectively, for winds higher than 5 m s^{-1}. Error propagation through COARE 3.0 results in uncertainties of the bulk fluxes listed in Table 2.

Thus far, we only accounted for measurement uncertainties that we were able to detect. As such, we assumed the current speed uncertainty to be equal to the current meter accuracy, namely, 0.01 m s^{-1} or 1%. If in fact there was a velocity shear due to waves, as discussed in section 4b, then the stress uncertainty would be near 20%. Similarly, assuming an additional bias of 0.2°C in SST and 0.25 g kg^{-1} in q_s, due to flow distortion below the buoy hull, uncertainties of hourly heat fluxes would be closer to 15% (latent) and 19% (sensible). For longwave and shortwave incoming radiations (LWR and SWR, respectively), cross-sensor differences are very small (about 1%–2% of mean values for hourly and daily averages). However, the platform tilt must bias the direct solar radiation compared to a level surface. We cannot quantify this effect since we measured only the global incoming SWR (sum of diffuse and direct components). But preliminary work following Long et al. (2010) and assuming 50% direct sunlight indicates it is less than 5%. Moreover, there are indications that ASIMET SWR used during CLIMODE had a low bias because of ageing of the paint on the calibration standard. Errors in the radiative fluxes are estimated at 5% for longwave and 10% for solar radiation. Overall, air–sea flux errors tend to be less than 20% when all these effects are included. Note that during high heat loss events, these errors become closer to 10%. However, uncertainty in the transfer coefficients should also be raised in such conditions since they are associated with high winds.

b. Comparison with DCFS fluxes

A goal of the CLIMODE program was to use the DCFS fluxes to improve bulk estimates of the fluxes and to reduce their overall uncertainty through refinement of the bulk transfer coefficients. As explained in section 3, the DCFS on the buoy produces DC estimates of the surface stress and buoyancy flux. The DCFS fluxes are then combined with mean ASIMET measurements to compute the drag and buoyancy flux transfer coefficients using Eqs. (6)–(8) and (2) as shown:

$$C_D = \frac{\tau}{\rho S(\overline{u}_s - \overline{u})}, \tag{16}$$

$$C_B = \frac{Q_B}{\rho c_{pa} S(\overline{T}_{vs} - \overline{\theta}_v)}, \tag{17}$$

where T_{vs} is surface value of T_v. The transfer coefficients are converted to their neutral values using the stability functions from COARE 3.0 as shown:

$$C_{DN} = \frac{C_D}{\left[1 + \dfrac{C_D^{1/2}\psi_u(z/L)}{\kappa}\right]^2}, \tag{18}$$

$$C_{BN} = C_{DN}^{1/2}\frac{C_B^{1/2}}{\left[1 + \dfrac{C_B^{1/2}\psi_\theta(z/L)}{\kappa}\right]}, \tag{19}$$

where the neutral values are denoted by N, and ψ_u and ψ_θ are the stability corrections for the wind and potential temperature profiles, respectively.

The neutral drag and buoyancy transfer coefficients are plotted against the neutral relative wind speed in Figs. 11 and 12. These values have been adjusted to 10 m to allow comparison with the formulation provided by Large and Pond (1981, 1982). The plotted wind speed covers the entire range of wind conditions for which the bulk transfer coefficients have been reported in the literature. These results are in good agreement with the COARE 3.0 drag coefficient parameterization for wind speeds between 6 and 14 m s^{-1}. However, there appear to be systematic departures from the COARE 3.0 drag coefficients at both low and high wind speeds. Recent investigations from the Coupled Boundary Layers and Air–Sea Transfer (CBLAST) program have reported similar results at low winds (Edson et al. 2007), where it has been hypothesized that the drag can be reduced in

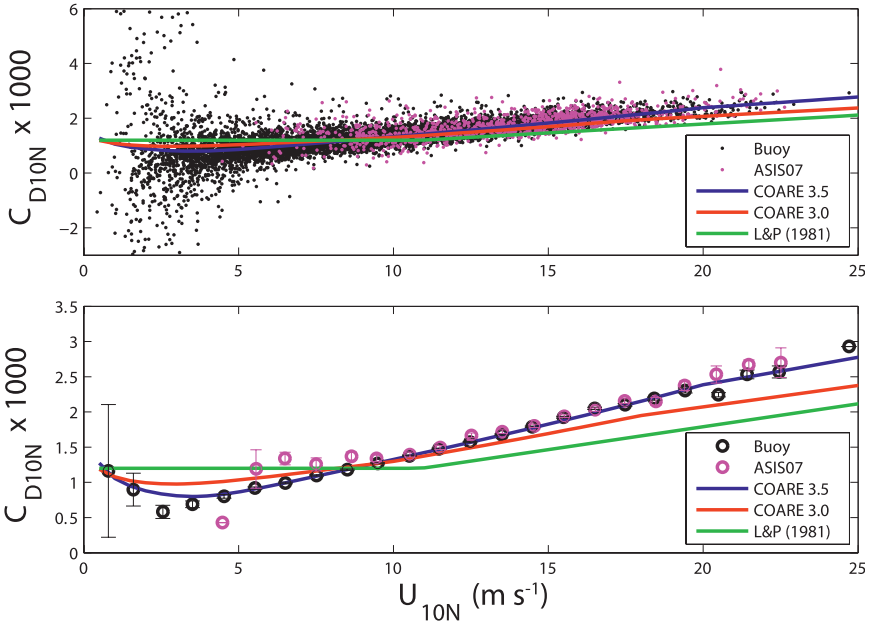

FIG. 11. (top) Individual estimates of the drag coefficient and (bottom) their averages within 1 m s^{-1} wind speed bins. The error bars in (bottom) represent the standard error. The coefficient has been adjusted to neutral conditions using the functions given by Fairall et al. (2003). Data are from CLIMODE F buoy (black dots or circles) and ASIS (magenta dots or circles). The red line is the COARE 3.0 formulation from Fairall et al. (2003), and the green line is the neutral drag efficient parameterization from Large and Pond (1981). The blue line represents a modification of the COARE 3.0 algorithm based on the CLIMODE data (COARE 3.5).

this regime due to the presence of swell (Sullivan et al. 2008). The buoy measurements show enhanced drag compared to COARE 3.0 at winds speeds above 14 m s^{-1}. These drag coefficients are significantly larger than the commonly used Large and Pond (1981) formulation, which is also lower than the COARE 3.0 algorithm.

The measured buoyancy transfer coefficients are in very good agreement with the COARE 3.0 algorithm at wind speeds up to 15 m s^{-1}. There is again a systematic departure from the COARE 3.0 at high winds. In this case, the measured transfer coefficients for the buoyancy flux are substantially lower than the COARE 3.0 prediction at wind speeds above 15 m s^{-1}. Although the comparison has focused on the buoy data, preliminary results from the air–sea interaction spar (ASIS) deployed during CLIMODE agree with these observations for both the drag and buoyancy flux transfer coefficients.

Therefore, the data are now being used to reduce the uncertainty in the transfer coefficients, particularly for wind speeds greater than 15 m s^{-1}. Work has begun to modify the COARE 3.0 algorithm to COARE version 3.5 (Edson et al. 2012, manuscript submitted to *J. Phys. Oceanogr.*). The main difference between the two versions is in the roughness length parameterization used for the drag coefficient and a slight modification with thermal roughness length to make the transfer coefficients agree with COARE 3.0 at low to moderate winds with reduced values at high winds. The latter is the subject of an ongoing investigation. The COARE 3.5 drag coefficient predicts slightly lower values of the stress at low winds and somewhat higher estimates of the stress at high winds. The COARE 3.5 buoyancy flux transfer coefficient is in close agreement with COARE 3.0 at low to moderate wind speeds and with Large and Pond (1982) at all wind speeds.

A comparison of the DC fluxes versus the three bulk algorithms investigated here are shown in Fig. 13. As expected, the agreement between the stress estimates shown in Fig. 13 is significantly improved at high winds through use of the COARE 3.5 parameterization. All three parameterizations give good agreement with the buoyancy fluxes shown in Fig. 13. However, again as expected, there is better overall agreement between the direct covariance and COARE 3.5 parameterization of the buoyancy flux.

An attempt to quantify the reduction of the uncertainty in these estimates is shown in Fig. 14. There, the mean and standard deviation of the difference between bulk and DC flux estimates are shown as a function of wind speed. The RMS normalized by the mean

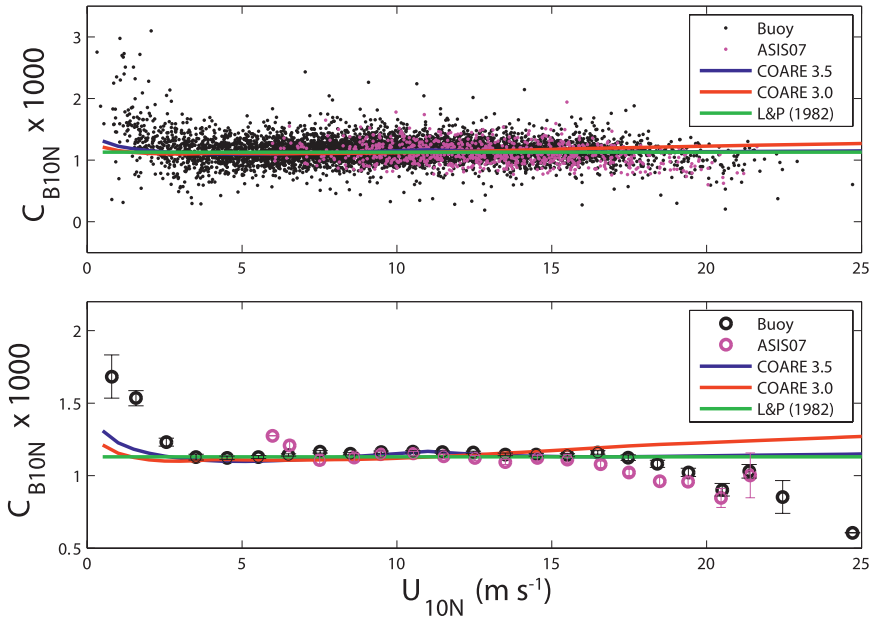

FIG. 12. (top) Individual estimates of the buoyancy flux transfer coefficient and (bottom) their averages within 1 m s^{-1} wind speed bins. The error bars in (bottom) represent the standard error. We have only plotted the transfer coefficients for the buoyancy flux when the absolute value of the air–sea virtual potential temperature difference exceeded 2°C. The coefficient has been adjusted to neutral conditions using the functions given by Fairall et al. (2003). Colors and symbols as in Fig. 11. The red line is the COARE 3.0 formulation from Fairall et al. (2003), and the green line is the neutral Stanton number parameterization for unstable conditions from Large and Pond (1982). The blue line represents a modification of the COARE 3.0 algorithm based on the CLIMODE data (COARE 3.5).

DC flux estimate is also shown and provides an estimate of the uncertainty of the fluxes. The uncertainty is computed for six wind speed bins incremented by 4 m s^{-1} between 0 and 24 m s^{-1}. This represents the combined uncertainty in the DC fluxes due to, for example, naturally occurring variability, flow distortion, and incomplete motion correction; and in the bulk fluxes due to, for example, missing physics in the parameterization (i.e., wave age and sea state) as well as the uncertainty in the mean measurements.

The uncertainty in the stress is greater than 100% at wind speeds below 5 m s^{-1}, due to the combined uncertainty and small value of the momentum flux. However, the plot shows a progressive improvement in the stress estimates where uncertainty in the COARE fluxes is less than 20% at moderate to high winds and approaches 10% for COARE 3.5. The uncertainty in the buoyancy flux is generally less than 30% for all parameterizations, for winds above 6 m s^{-1}. This uncertainty is in remarkably good overall agreement with the error analysis given in section 5a and shown in Fig. 10. This suggests that a substantial fraction of the uncertainty shown in Fig. 14 is due to random errors and errors in the bulk method. This provides additional evidence that accurate direct covariance flux estimates are possible from surface moorings and that these results can be used to improve the bulk formula.

Last, the COARE 3.0 and 3.5 parameterizations both show an increasing uncertainty in buoyancy flux at high winds, consistent with the results shown in Fig. 12. Under these conditions, a number of studies have shown that evaporating sea spray begins to have a noticeable impact on the heat exchange (Andreas et al. 1995). However, the contribution of both latent and sensible heat exchange between the droplets and atmosphere make it difficult to determine the impact of sea spray using the buoyancy flux alone. Therefore, the buoyancy flux estimates from the buoy and other platforms are now being combined with latent heat fluxes to investigate the Stanton and Dalton numbers directly.

6. Conclusions

A surface mooring was successfully deployed for almost 15 months in the Gulf Stream region and allowed the continuous collection of air–sea measurements. This

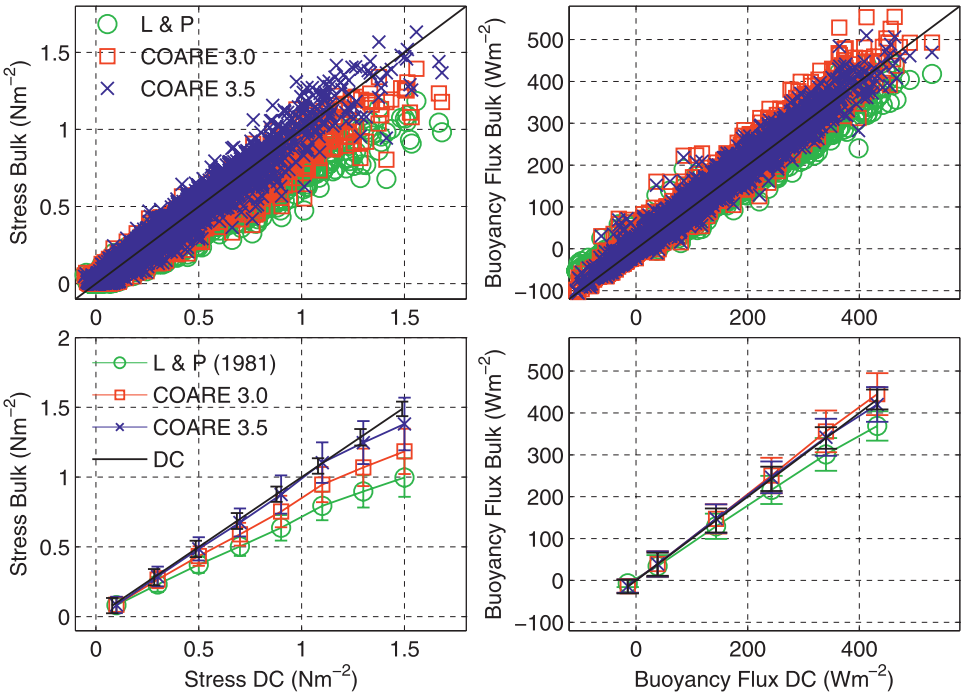

FIG. 13. A comparison between DC and estimates from commonly used bulk formulas. (left) Momentum flux (stress) and (right) buoyancy flux [from Eq. (2)]. (top) Scatterplots of bulk estimates using Large and Pond 1981 (green circles), COARE 3.0 (Fairall et al. 2003, red squares), and a new improved version COARE 3.5 (Edson et al. 2012, manuscript submitted to *J. Phys. Oceanogr.;* blue crosses) vs DC measurements. Black line is a 1:1 relationship. (bottom) Binned data from scatterplots above (bin size is 0.2 N m^{-2} and 100 W m^{-2} for stress and buoyancy flux, respectively); symbols denote the average bulk value, and vertical bars denote the corresponding standard deviation inside each bin.

paper focused on the uncertainties in the observations and how these uncertainties impacted the goal of observing the air–sea fluxes. Pre- and postdeployment calibrations together with in situ comparison between shipboard and moored sensors supported identification of biases due to sensor drifts, sensor electronics, and calibration errors. A postdeployment field study was used to further investigate the performance of the wind sensors. The use of redundant sensor sets not only filled data gaps but also provided a means to examine the contribution of random errors.

In some cases, for air temperature and humidity, barometric pressure, and rain rate, the errors in the mean meteorological observations in this challenging environment were not significantly larger than those reported by Colbo and Weller (2009) for subtropical conditions. Calibration and instrumentation electronics errors were dealt with in incoming shortwave radiation and incoming longwave radiation, respectively. Better quantification of the error in observed rain rates was not possible. A significant effort was directed at a better definition of errors in wind speed. Flow distortion was quantified in the observations and was consistent with CFD simulations (Edmond et al. 2012). An empirical correction was proposed to reduce the low bias in wind speed estimates from 2D sensors like the ASIMET. We estimate that this low bias is less than 5% for winds less than 15 m s^{-1} and less than 10% for higher winds.

The propagation of the observation errors in the bulk formulas allowed us to develop figures showing the error in these fluxes as a function of wind speed and air–sea temperature difference. These propagated errors asymptote to lower values in high wind speeds to about 12% in latent heat flux, 10% in sensible heat flux, and 15% in wind stress. However, an additional uncertainty stems from use of the bulk formulas. To investigate this, direct covariance fluxes were compared with the bulk formulas. Between 6 and 15 m s^{-1}, there was good agreement between the COARE 3.0 bulk formula momentum fluxes and the DCFS momentum fluxes. At both lower and higher wind speeds, there were systematic departures in the drag coefficients. These are now being addressed through a modification to the COARE algorithm using CLIMODE data. Below 15 m s^{-1}, the buoyancy fluxes were in good agreement. But above 15 m s^{-1}, the DCFS buoyancy fluxes were lower than the COARE 3.0 buoyancy fluxes. Additional biases may

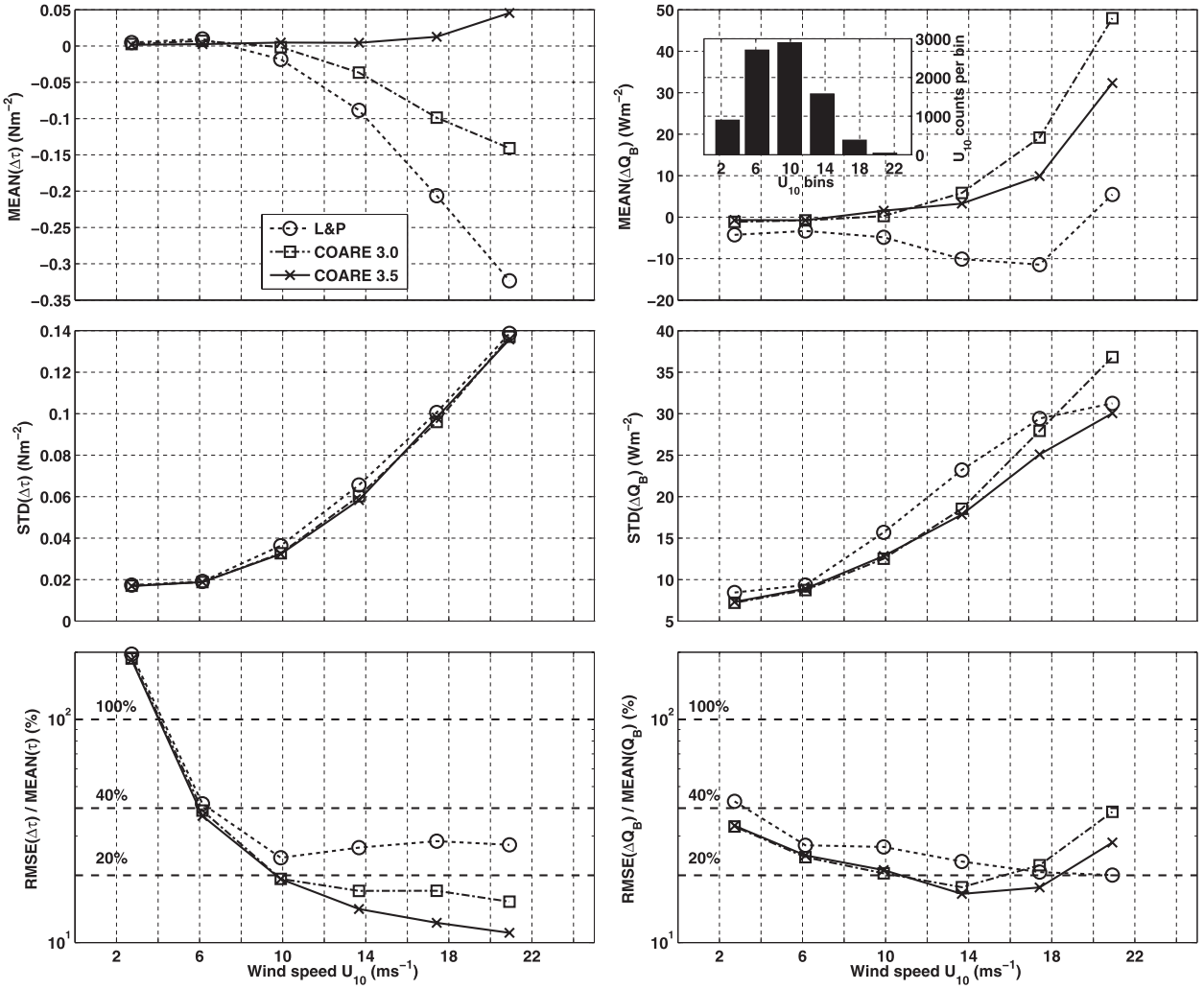

FIG. 14. Statistics of flux difference bulk estimates minus DC measurements as a function of wind speed. (left) Momentum flux and (right) buoyancy flux. (top) Mean of flux difference for wind speed data in 4 m s^{-1} bins (see inset in top-right plot for histogram of wind speed bins). (middle) Standard deviation inside each bin. (bottom) RMS of the difference inside each bin, divided by the mean DC flux value inside the bins in percent.

exist but could not be directly quantified that affect interface values of T_s, q_s, and U_s. We attempted to account for these biases in the flux errors, which remained close to or less than 20%.

Thus, our basic conclusion is that the surface buoy deployed in the Gulf Stream to support air–sea interaction research was successful, providing an improved 15-month record of surface meteorology, upper-ocean variability, and air–sea fluxes with known accuracies. At the same time, the coincident deployment of mean meteorological and turbulent flux sensors proved to be a successful strategy to certify the validity of the bulk formula fluxes over the midrange of wind speeds and to support further work to address the present shortcomings of the bulk formula methods.

Acknowledgments. The National Science Foundation (Grant OCE04-24536) funded this work, as part of the CLIVAR Mode Water Dynamics Experiment (CLIMODE). The Vetlesen Foundation is also acknowledged for the early support of S. Bigorre. We thank Al Plueddemann and Tom Farrar (WHOI) for discussions of the uncertainties in the wind observations. Many thanks to Frank Bradley and Chris Fairall, who kindly provided their code for COARE 3 bulk flux errors. The personnel of the Upper Ocean Processes Group (WHOI), who designed, calibrated, maintained, and deployed most components of the surface mooring and its instrumentation, are deeply appreciated. Finally, we thank the three anonymous reviewers, whose constructive comments helped improve this manuscript.

REFERENCES

Andreas, E. L, J. B. Edson, E. C. Monahan, M. P. Rouault, and S. D. Smith, 1995: The spray contribution to net evaporation from the sea: A review of recent progress. *Bound.-Layer Meteor.,* **72,** 3–52.

Bane, J. M., Jr., and K. E. Osgood, 1989: Wintertime air-sea interaction processes across the Gulf Stream. *J. Geophys. Res.,* **94** (C8), 10 755–10 722.

Blanton, J. O., J. A. Amft, D. K. Lee, and A. Riordan, 1989: Wind stress and heat fluxes observed during winter and spring 1986. *J. Geophys. Res.,* **94** (C8), 10 686–10 698.

Bradley, E. F., and C. W. Fairall, 2006: A guide to making climate quality meteorological and flux measurements at sea. NOAA Tech. Memo. OAR PSD-311, 107 pp.

Colbo, K., and R. A. Weller, 2009: The accuracy of the IMET sensor package in the subtropics. *J. Atmos. Oceanic Technol.,* **9,** 1867–1890.

Cronin, M. F., and Coauthors, 2010: Monitoring ocean-atmosphere interactions in western boundary current extensions. *Proceedings of OceanObs'09: Sustained Ocean Observations and Information for Society,* J. Hall, D. E Harrison, and D. Stammer, Eds., Vol. 2, ESA Publ. WPP-306, doi:10.5270/OceanObs09.cwp.20.

Edmond M., D. Vandemark, J. Forsythe, A. J. Plueddemann and J. T. Farrar, 2012: Flow distortion investigation of wind velocity perturbations for two ocean meteorological platforms. Woods Hole Oceanographic Institution Tech. Rep. WHOI-2012-02, 66 pp.

Edson, J. B., A. A. Hinton, K. E. Prada, J. E. Hare, and C. W. Fairall, 1998: Direct covariance flux estimates from mobile platforms at sea. *J. Atmos. Oceanic Technol.,* **15,** 547–562.

——, and Coauthors, 2007: The coupled boundary layers and air–sea transfer experiment in low winds. *Bull. Amer. Meteor. Soc.,* **88,** 341–356.

Fairall, C. W., E. F. Bradley, D. P. Rogers, J. B. Edson, and G. S. Young, 1996: Bulk parameterization of air-sea fluxes for Tropical Ocean-Global Atmosphere Coupled-Ocean Atmosphere Response Experiment. *J. Geophys. Res.,* **101** (C2), 3747–3767.

——, ——, J. Hare, A. Grachev, and J. Edson, 2003: Bulk parameterization of air–sea fluxes: Updates and verification for the COARE algorithm. *J. Climate,* **16,** 571–591.

Gobat, J. I., and M. A. Grosenbaugh, 2000: WHOI Cable v2.0: Time domain numerical simulation of moored and towed oceanographic systems. Woods Hole Oceanographic Institution Tech. Rep. WHOI-2000-08, 83 pp.

Hasselmann, K., W. Sell, D. B. Ross, and P. Müller, 1976: A parametric wave prediction model. *J. Phys. Oceanogr.,* **6,** 200–228.

Hosom, D. S., R. A. Weller, R. E. Payne, and K. E. Prada, 1995: The IMET (improved meteorology) ship and buoy systems. *J. Atmos. Oceanic Technol.,* **12,** 527–540.

Konda, M., H. Ichikawa, H. Tomita, and M. F. Cronin, 2010: Surface heat flux variations across the Kuroshio as observed by surface flux buoys. *J. Climate,* **23,** 5206–5221.

Kubota, M., N. Iwabe, M. F. Cronin, and H. Tomita, 2008: Surface heat fluxes from the NCEP/NCAR and NCEP/DOE reanalyses at the Kuroshio Extension Observatory buoy site. *J. Geophys. Res.,* **113,** C02009, doi:10.1029/2007JC004338.

Large, W. G., and S. Pond, 1981: Open ocean momentum flux measurements in moderate to strong winds. *J. Phys. Oceanogr.,* **11,** 324–336.

——, and ——, 1982: Sensible and latent heat flux measurements over the ocean. *J. Phys. Oceanogr.,* **12,** 464–482.

Long, C. N., A. Bucholtz, H. Jonsson, B. Schmid, A. M. Vogelmann, and J. Wood, 2010: A method of correcting for tilt from horizontal in downwelling shortwave irradiance measurements on moving platforms. *Open Atmos. Sci. J.,* **4,** 78–87, doi:10.2174/1874282301004010078.

Marshall, J., and Coauthors, 2009: Observing the cycle of convection and restratification over the Gulf Stream system and the subtropical gyre of the North Atlantic Ocean: Preliminary results from the CLIMODE field campaign. *Bull. Amer. Meteor. Soc.,* **90,** 1337–1350.

Minobe, S., A. Kuwano-Yoshida, N. Komori, S.-P. Xie, and R. J. Small, 2008: Influence of the Gulf Stream on the troposphere. *Nature,* **452,** 206–209.

Moore, G. W. K., and I. A. Renfrew, 2002: An assessment of the surface turbulent heat fluxes from the NCEP–NCAR reanalysis over the western boundary currents. *J. Climate,* **15,** 2020–2037.

Renfrew, I. A., G. W. K. Moore, P. S. Guest, and K. Bumke, 2002: A comparison of surface layer and surface turbulent flux observations over the Labrador Sea with ECMWF analyses and NCEP reanalyses. *J. Phys. Oceanogr.,* **32,** 383–400.

Serra, Y. L., and M. J. McPhaden, 2003: Multiple time- and space-scale comparisons of ATLAS buoy rain gauge measurements with TRMM satellite precipitation measurements. *J. Appl. Meteor.,* **42,** 1045–1059.

——, P. A'Hearn, H. P. Freitag, and M. J. McPhaden, 2001: ATLAS self-siphoning rain gauge error estimates. *J. Atmos. Oceanic Technol.,* **18,** 1989–2002.

Shaw, W. J., 1990: Theory and scaling of lower atmospheric turbulence. *Surface Waves and Fluxes: Current Theory,* G. L. Geernaert and W. J. Plant, Eds., Environmental Fluid Mechanics, Vol. 1, Kluwer Academic Publishers, 63–72.

Sullivan, P. P., J. B. Edson, T. Hristov, and J. C. McWilliams, 2008: Large-eddy simulations and observations of atmospheric marine boundary layers above nonequilibrium surface waves. *J. Atmos. Sci.,* **65,** 1225–1245.

Weller, R. A., and S. P. Anderson, 1996: Surface meteorology and air–sea fluxes in the western tropical Pacific warm pool during the TOGA Coupled Ocean–Atmosphere Response Experiment. *J. Climate,* **9,** 1959–1990.

——, S. P. Bigorre, J. Lord, J. D. Ware, and J. B. Edson, 2012: A surface mooring for air–sea interaction research in the Gulf Stream. Part I: Mooring design and instrumentation. *J. Atmos. Oceanic Technol.,* **29,** 1363–1376.

Yamartino, R. J., 1984: A comparison of several ''single-pass'' estimators of the standard deviation of wind direction. *J. Climate Appl. Meteor.,* **23,** 1362–1366.

Yang, D., B. E. Goodison, J. R. Metcalfe, V. S. Golubev, R. Bates, T. Pangburn, and C. L. Hanson, 1998: Accuracy of NWS 8″ standard nonrecording precipitation gauge: Results and application of WMO intercomparison. *J. Atmos. Oceanic Technol.,* **15,** 54–68.

Yu, L., R. A. Weller, and B. Sun, 2004: Improving latent and sensible heat flux estimates for the Atlantic Ocean (1988-1999) by a synthesis approach. *J. Climate,* **17,** 373–393.

Zhang, N. F., 2006: Calculation of the uncertainty of the mean of autocorrelated measurements. *Metrologia,* **43,** S276, doi:10.1088/0026-1394/43/4/S15.

Zięba, A., 2010: Effective number of observations and unbiased estimators of variance for autocorrelated data - An overview. *Metrol. Meas. Syst.,* **17,** 3–16.